JGR Solid Earth

RESEARCH ARTICLE
10.1029/2021JB022251

Tidal Triggering of Microseismicity at the Equatorial Mid-Atlantic Ridge, Inferred From the PI-LAB Experiment

K. Leptokaropoulos[1], N. Harmon[1], S. P. Hicks[2], C. A. Rychert[1], D. Schlaphorst[3], and J. M. Kendall[4]

[1]Ocean and Earth Science, University of Southampton, Southampton, UK, [2]Department of Earth Science and Engineering, Imperial College London, London, UK, [3]Instituto Dom Luiz (IDL), Faculdade de Ciências, Universidade de Lisboa, Lisbon, Portugal, [4]Department of Earth Sciences, University of Oxford, Oxford, UK

Key Points:

- Tidal triggering is investigated for a microseismicity data set from the equatorial Mid-Atlantic Ridge
- Seismicity rates are increased and b-values are decreased during and towards low tides
- Coulomb stress modeling suggests additional factors are required, for example, a shallow magma chamber beneath the ridge

Supporting Information:

Supporting Information may be found in the online version of this article.

Correspondence to:

K. Leptokaropoulos,
K.Leptokaropoulos@soton.ac.uk

Citation:

Leptokaropoulos, K., Harmon, N., Hicks, S. P., Rychert, C. A., Schlaphorst, D., & Kendall, J. M. (2021). Tidal triggering of microseismicity at the equatorial Mid-Atlantic Ridge, inferred from the PI-LAB experiment. *Journal of Geophysical Research: Solid Earth*, *126*, e2021JB022251. https://doi.org/10.1029/2021JB022251

Received 16 APR 2021
Accepted 25 AUG 2021

Abstract The gravitational pulls from the moon and the sun result in tidal forces which influence both Earth's solid and water mass. These stresses are periodically added to the tectonic ones and may become sufficient for initiating rupture in fault systems critically close to failure. Previous research indicates correlations between increased seismicity rates and low tides for fast- and intermediate-spreading mid-ocean ridges in the Pacific Ocean. Here, we present a microseismicity data set (4,719 events) recorded by an ocean bottom seismometer deployment at the equatorial Mid-Atlantic Ridge. We show that low, as well as decreasing ocean water level, result in relatively elevated seismicity rates at higher magnitudes (lower b-values), translated into increased probabilities of stronger event occurrence at or towards low tides. Moreover, seismic bursts (enhanced activity rate clusters), occurring at rates well above the reference seismicity, are exclusively present during values of either high tidally induced extensional stresses or high extensional stress rates. Although the b-value differences are not significant enough to be conclusive, the seismicity rate variations exhibit statistical significance, supporting the previous findings for tidal triggering at low tides within normal-faulting regimes and extending the range of observations to slow-spreading ridges. Observed triggering of slip on low angle faults at low tides is predicted by Coulomb stress modeling. The triggering of slip on high angle faults observed here, is not easily explained without another factor. It may be related to the presence of a shallow magma body beneath the ridge, as supported by previous seismic imaging in the region.

Plain Language Summary The Earth is periodically subjected to tidal forces due to the combined influence of solar and lunar gravity. Solid Earth tides dominate in the continents, whereas in particular marine sites ocean tides are strong enough to generate considerable stress. Although theoretically plausible, tidal triggering of earthquakes has been only occasionally observed in the Pacific Ocean, with the results often being controversial. The deployment of ocean bottom seismometers (OBS) in combination with modern earthquake detection techniques, offer better chances to study the remote oceanic environments, making it possible to recognize a tidal footprint on small earthquakes. Here we present a dense data set of small earthquakes from the equatorial Mid-Atlantic Ridge, recorded by a temporary OBS network operated from March 2016 to February 2017. We find that the majority of the earthquakes occurred during or towards low tides, corresponding to high extensional stressing. We show that seismicity bursts (very high activity rates) exclusively occur at low tides. There is also evidence that a larger proportion of stronger events occur during or just before low tides. We interpret our results in terms of stress change modeling, considering faulting properties and the potential existence of a magma chamber beneath the study area.

1. Introduction

Oceanic plates cover the majority of Earth's surface, and mid-ocean ridges (MOR), the active boundaries of two divergent oceanic plates play a major role in global plate tectonics. New lithosphere is created along oceanic spreading centers by a combination of tectonic and magmatic processes, as molten rock emerges from the upper mantle beneath (Hofmann, 1997). Recently, Agius et al. (2021) showed that deep material transfer from lower to upper mantle is also linked to spreading processes along the equatorial Mid-Atlantic

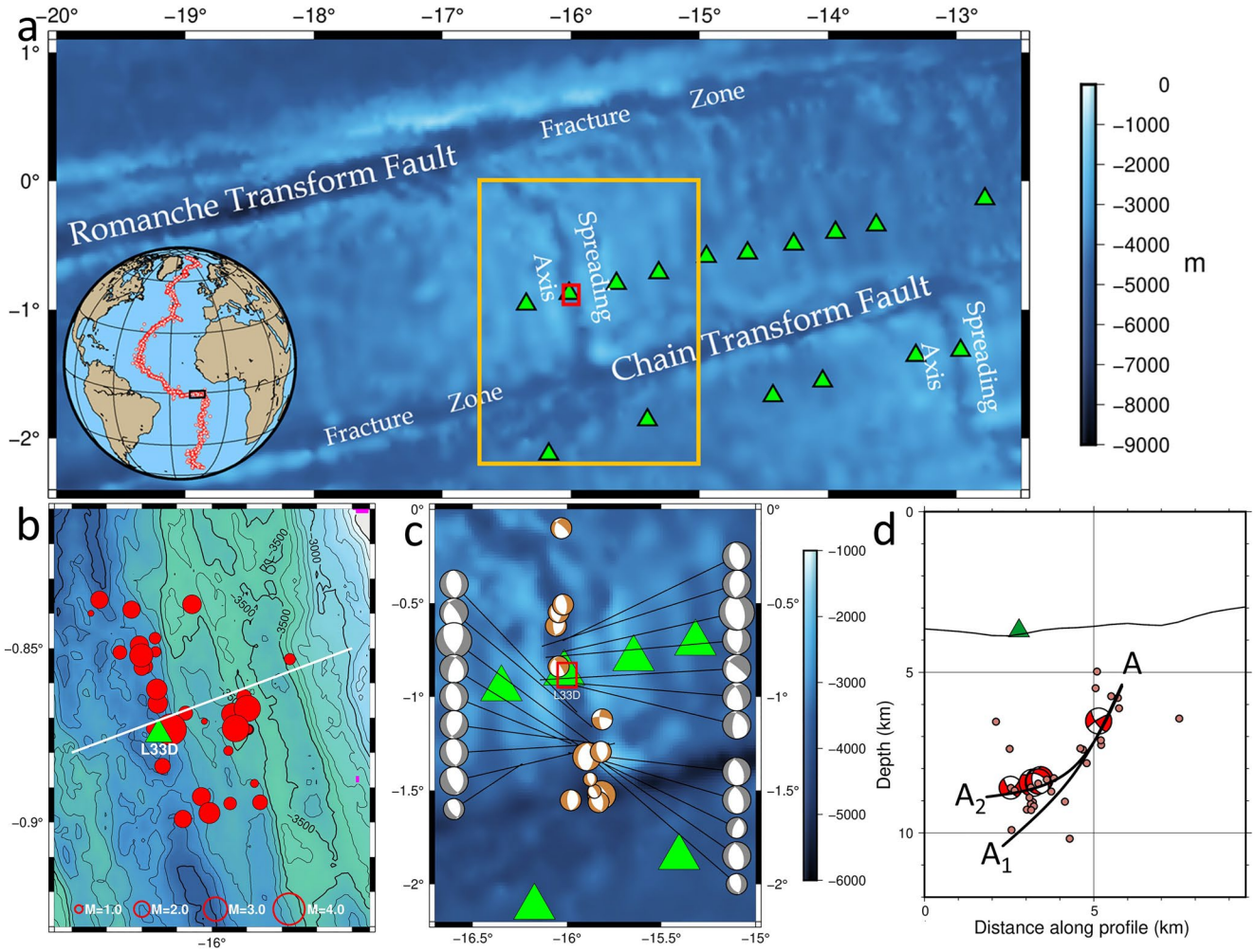

Figure 1. (a) Regional map of equatorial Atlantic with bathymetry and main morphological features indicated: Chain and Romanche transform faults; their corresponding fracture zones; the Mid-Atlantic Ridge (MAR) spreading axes. The small red rectangle shows the study area magnified in (b). The large yellow rectangle shows the broader area magnified in (c). The inset map indicates the location of (a) in Atlantic Ocean (black rectangle) and MAR global seismicity since 1964. Locations of $M \geq 5$, earthquakes from Teza et al. (2016) are shown as red circles. Green triangles in all panels denote the location of ocean bottom seismometers stations operated during the PI-LAB experiment. (b) Bathymetric map of the study area. The red circles indicate the 34 seismicity templates used to compile the catalog in the study. The gray line indicates the cross-section shown in (d). The closest station, L33D is labeled. (c) Broader area focused on the ridge spreading axis shown in (a). The red rectangle shows the study area, magnified in (b). The focal mechanisms from the Global Centroid Moment Tensor (GCMT, Ekström et al., 2012; gray) and this study (brown) are shown as lower hemisphere projections. (d) Double difference locations of selected events (34 templates), plotted along a ridge-perpendicular cross-section shown in (b), suggesting possible reactivations of a west-dipping normal fault. Plausible high angle (Line A-A1) or listric (Line A-A2) fault geometries are shown. The available focal mechanisms projected onto the cross-section, and L33D station (green triangle) are also depicted in cross-section view.

Ridge (MAR), thus ridge upwellings may compensate slab downwellings in subduction zones. The MAR is Earth's longest mountain chain extending from the Arctic down to the Bouvet Triple Junction in South Atlantic and is characterized as a slow spreading ridge (full spreading rate <40 mm/yr). Volcanic activity is also evident as well as shallow seismicity, often occurring as swarms (e.g., Sykes, 1970). This long belt is not continuous but fragmented by a system of dextral and sinistral transform faults (TF), perpendicular to the ridge (Macdonald, 2001). Seismicity along the MAR provides evidence for the nature of the processes that govern the composition and dynamics of the oceanic lithosphere. Normal faulting is predominantly observed along the ridge, with earthquake magnitudes rarely exceeding $M_W = 6.0$. Strike-slip faulting with one nodal plane parallel to the TF strike is the dominant mechanism along the TFs.

Our study area is a segment of the equatorial MAR located at ~1°S and 16°W (Figure 1), between the Chain and Romanche TFs. Both TFs and the ridge segment they offset were previously mapped, although more

for physical oceanographic purposes (e.g., Mercier & Morin, 1997; Mercier & Speer, 1998). In March 2016, 39 ocean bottom seismometers (OBS) were deployed at both sides of the MAR, centered on the Chain Transform Zone, under the framework of the Passive Imaging of the Lithosphere-Asthenosphere Boundary (PI-LAB) and the Experiment to Unearth the Rheological Lithosphere-Asthenosphere Boundary experiments (EURO-LAB). The network operated for 1 year and the data acquired were used, in combination with other geophysical measurements, in a variety of studies focused on sediment structure (Agius et al., 2018; Saikia et al., 2020), infragravity wave sources (Bogiatzis et al., 2020), a multidisciplinary marine geophysical investigation of the active transform valley, the adjacent spreading segments and oceanic lithosphere (e.g., Harmon et al., 2018, 2020, 2021; Rychert et al., 2020, 2021; Saikia et al., 2021; Wang et al., 2020), deeper imaging of thinning of the mantle transition zone (Agius et al., 2021),and a high-resolution study of a $M_W = 7.1$ earthquake on the nearby Romanche TF (Hicks et al., 2020). Here, we use the data gathered within the duration of the PI-LAB experiment, in order to study the properties and triggering mechanisms of microseismicity that occurred in the equatorial segment of the MAR.

Several of the proposed mechanisms of seismic activity across MORs are related to the thermal profile and regard frictional weakening occurring in high-temperature (e.g., geothermal) extensional regimes (e.g., Hough & Kanamori, 2002), hydrothermal circulation (e.g., Behn et al., 2007), and hydrothermal alteration (serpentinization) which considerably lowers rock strength (e.g., Escartin et al., 2001). In addition, oceanic faults are subjected to a permanent seawater overburden, which produces considerable tidal effects. The solar and lunar gravitational interaction with the Earth induces oscillatory stresses at semi-diurnal (~12h), diurnal (~24h) and even longer periods (e.g., fortnightly, ~14.7 days). Although the tidal stresses (kPa) are ~3 orders of magnitude lower than tectonic stresses (MPa), the rate of tidal stressing may be comparable to or exceed that of tectonic stressing by up to 2 orders of magnitude (Heaton, 1975; Wilcock et al., 2016). In addition, since tides are periodic and their effect can be accumulated in time, they provide a useful tool for investigating potential earthquake triggering.

There are several studies suggesting tidal triggering at MORs (e.g., Bhatnagar et al., 2015; Stroup et al., 2007; Tan et al., 2019; Tolstoy et al., 2002; Wilcock, 2001; Wilcock et al., 2016). These studies have focused on intermediate (Juan de Fuca) and fast (East Pacific Rise) spreading ridges and less attention has been paid to slow spreading ridges such as the MAR. Although there are some microseismicity studies for various MAR segments (e.g., Grevemeyer et al., 2013; Horning et al., 2018; Parnell-Turner et al., 2017, 2020), temporal variations in seismicity, such as tidal effects and triggering mechanisms have not been fully investigated along the MAR. Tidal pressure was shown to modulate high temperature hydrothermal discharge at the Lucky Strike deep sea vent field at 37°N, although seismicity was only briefly discussed (Barreyre et al., 2014).

Summarizing the findings of the previous research, there are four major characteristics of tidal triggering in oceanic environments:

1. *Tectonic setting*. Tidal triggering has been identified in normal (e.g., Scholz et al., 2019; Tanaka et al., 2002; Tsuruoka et al., 1995) and reverse (e.g., Cochran et al., 2004; Ide et al., 2016; Tanaka et al., 2002) faulting regimes. Tidal effects appear essentially absent in any strike-slip fault systems (e.g., Tanaka et al., 2002; Tsuruoka et al., 1995; Vidale et al., 1998).
2. *Tidal characteristics*. Ocean tides induce stresses an order of magnitude larger than solid Earth tides (Cochran et al., 2004; Tsuruoka et al., 1995; Wilcock, 2009). An exception is at 9°50'N on the East Pacific Rise, which is located within an ocean tidal node, resulting in the dominance of solid Earth over ocean tides (Bhatnagar et al., 2015; Stroup et al., 2007).
3. *Timing*. Vertical tidal stress also dominates and is in phase with the ocean tides (e.g., Scholz et al., 2019; Wilcock, 2001), such that the vertical component (directly connected to ocean height) can be mainly considered.
4. *Optimum receiver fault geometry*. Particularly at MORs, triggering on normal faults is associated with low tides, which correspond to the maximum extensional stress (e.g., Tolstoy et al., 2002; Tsuruoka et al., 1995; Wilcock et al., 2016). This is generally inconsistent with the predicted Coulomb stress at low tides for high angle normal faults. However, it could be consistent with Coulomb stresses that would unclamp (Wilcock et al., 2016) low angle normal faults, that is, that could exist if the MOR faults are listric in shape. Alternatively, additional influences such as magmatic inflation from below have been suggested (Scholz et al., 2019).

In this study, we use the seismicity data acquired by the PI-LAB and EURO-LAB projects to investigate the role of tides as a triggering mechanism of microseismicity along a segment of the equatorial MAR. We investigate the correlation between ocean tide phase and amplitude with the occurrence of seismicity. Then, we identify seismic sequences characterized by enhanced activity rates (i.e., temporal clusters) separated by time periods in which seismic activity falls well below the reference seismicity level. We also demonstrate how the magnitude distribution of seismicity is influenced by tidal fluctuations. Finally, we interpret the results in terms of Coulomb stress changes and extract information on frictional and hydraulic properties of the lithosphere in the close vicinity of the axial ridge.

2. Materials and Methods

2.1. Seismicity Data

We use continuous waveform data from the PI-LAB OBS stations and apply "lassie" (Heimann et al., 2017), a stack-and-delay based waveform coherence detector, to find and locate seismic events. In this method, coherency is mapped using a smooth characteristic function calculated from normalised envelopes. We specifically target events within a radius of ∼25 km from station L33D, which is located in the axial valley (Figure 1). Such a limited radius was used to ensure that the events were located in the vicinity of L33D with robust depth resolution, and also to minimize the likelihood of detecting seismicity along the adjacent TFs.

Following manual picking of P- and S-wave arrival times in detected events, we then relocate these events with a probabilistic non-linear approach using the NonLinLoc software (Lomax et al., 2000). We use a 1-D V_p model based on CRUST1.0 (Laske et al., 2013). We select a fixed V_p/V_s ratio of 1.74 based on a linear fit to a modified Wadati plot (e.g., Chatelain et al., 1980). This yielded a total of 48 well-located events (azimuthal gap < 220°; >4 P-wave picks; >3 S-wave picks; maximum depth error, within 68% confidence interval, <5 km). The average RMS residual of these events is ∼0.08 s, suggesting well-constrained locations and minimal unmodelled velocity deviations from the 1-D approximation. We compute event magnitudes by taking the three-component maximum amplitude and computing single-station local magnitudes (M_L) at station L33D using the relationship derived by Bakun and Joyner (1984) (Figure S1a).

For higher-precision earthquake locations, we use the double-difference method (Waldhauser & Ellsworth, 2000) that uses our phase arrival times and higher-precision cross-correlation measurements for P- and S- waves on a window of 2.5–18 Hz bandpass-filtered data starting 0.1 s before and ending 0.2 s after our picked arrival time. We allow a maximum cross-correlation lag of 0.1 s and a minimum allowed cross-correlation coefficient of 0.4. This double-difference relocation resulted in a single cluster of 34 events located within a ∼5 km distance from L33D station (Figure 1b), with a mean depth error of ∼200 m indicating a distinct group of events lying at 5–10 km depth beneath sea level (Figure 1d). The shallower events, to the side of the axial valley, appear to form a lineation in seismicity, which dips at a moderate angle to the west. A tight cluster of events lies directly beneath the axial valley at 8–10 km depth below sea level. Visual analysis of waveforms at ridge station L33D shows that recordings of small, local seismic events (S-P differential time of <2 s) are very common, with tens of these signals showing up in a typical day. However, many of these events cannot be identified on other stations due to their low magnitude and possible strong path attenuation, as would be needed for network-based detection and relocation.

To further investigate microseismicity along the ridge segment, we mostly rely on single-station detection at L33D. We use waveform template matching to study the ridge microseismicity, which allows detection of events within noise (e.g., Gibbons & Ringdal, 2006). From three-component waveforms of the double-difference relocated events, we form event templates. We used our catalog of 34 events as templates used for the matched filter-detection using the EQcorrscan software package (Chamberlain et al., 2018). Templates are bandpass-filtered between 2 and 20 Hz, which includes much of the energy of these local seismic events, and minimizes the effect of ocean noise (Figures S1c and S1d). Templates are 1.4 s long, beginning 0.1 s before the picked arrival time (Figure S1b). P-wave templates are constructed on the vertical component, whereas S-waves come from the horizontal components. Thresholding is based on the mean-values of cross-correlations from each of L33D's components. Visual analysis of waveforms from a subset of detected events shows that an average channel correlation detection threshold of 0.65 is suitable. This value is similar to other studies using single-station template matching (e.g., Vuan et al., 2018). We then check

for, and remove, duplicate detections (within 20 s) and select the template detection with the greatest mean cross-correlation value. This workflow led us to the identification of 4,719 events with magnitudes ranging from M_L −1.4 to M_L 4.0. However, we note that the resulting M_L is based on a single-station estimates. Therefore, there is considerable uncertainty incorporated in these estimates. In addition, it is unknown how M_L scales with M_W, since almost all events in our catalog are too weak for moment tensor inversion and spectral fitting.

The moment tensor solutions are calculated using the local seismicity catalog. The hypocenter depths and focal mechanisms are computed using Bayesian-bootstrap time-domain deviatoric moment tensor inversion in Grond (see Heimann et al., 2018 for further details). The data is inverted in the frequency range of 12–25 s. The previously derived lateral location is kept fixed and for the inversion only the vertical traces are used. The solutions presented in this work represent the double-couple component of the focal mechanism, since the station coverage is not able to resolve potential non-double couple faulting components. The uncertainties in centroid depth and focal mechanism parameters are representations of the probability density functions derived from bootstrapping chains. Due to noise and event magnitude constraints, focal mechanisms could only be obtained for five of the events in the study area (Figure 1d) and 12 events along the entire ridge segment (Figure 1c). Most of these 12 events have magnitudes above 4.5 and thus it is virtually impossible to calibrate a specific M_L scale for our study area in which $-1.4 < M_L < 4.0$.

2.2. Tidal Stresses

The SPOTL software (Agnew, 1997) is used to calculate solid Earth tides as well as ocean loading with the global ocean tide model TPXO72.2010, produced by Oregon State University (see Egbert & Erofeeva, 2002). The predicted tidal heights are estimated by incorporating the tidal constituents M2, N2, S2, K2, K1, P1, O1 Q1, and M4 (Agnew, 1997 and references therein). The vertical stress can be then derived directly from the ocean tide height, given the water density, ρ, and the gravity acceleration, g, as:

$$\Delta\sigma_Z = g\rho h \tag{1}$$

Whereas the horizontal stresses induced by ocean tides ($\Delta\sigma_{Xo}$ and $\Delta\sigma_{Yo}$), assuming uniaxial strain, can be expressed as:

$$\Delta\sigma_{Xo} = \Delta\sigma_{Yo} = \frac{v}{1-v}\Delta\sigma_Z \tag{2}$$

where, v is the Poisson ratio. The corresponding horizontal stresses due to the solid Earth tides ($\Delta\sigma_{Xe}$ and $\Delta\sigma_{Ye}$) are:

$$\Delta\sigma_{Xe} = \frac{E}{1-v^2}\left(\Delta\varepsilon_X + v\Delta\varepsilon_Y\right), \Delta\sigma_{Ye} = \frac{E}{1-v^2}\left(\Delta\varepsilon_Y + \Delta\varepsilon_X\right) \tag{3}$$

where $\Delta\varepsilon_X$ and $\Delta\varepsilon_Y$, are the horizontal tidal normal strains, calculated by SPOTL and E, is Young's modulus. Solid Earth tides do not alter the vertical stress just below the ocean floor and thus, we assume that Equation 1 is a sufficient approximation of vertical stress change at shallow depths (e.g., Wilcock, 2009). The horizontal stresses induced by ocean tides have amplitudes comparable to the corresponding ones produced by solid Earth tides and they usually lag almost half a cycle. As a result, they compensate each other and thus, total horizontal stresses are roughly an order of magnitude smaller than the vertical stress induced by the water column fluctuations at most times (Figures S2 and S3). Given a fault with dip, δ and rake, λ, the contribution of tidal loading changes in the Coulomb failure stress, ΔCFS, (e.g., Harris, 1998) is given as:

$$\Delta\text{CFS} = \Delta\tau + \mu\left(\Delta\sigma_n + \Delta P\right) \tag{4}$$

whereas the shear stress acting on the fault plane, Δτ, can be expressed as:

$$\Delta\tau = \Delta\sigma_Z\left(\frac{2v-1}{1-v}\right)\sin\lambda\cdot\sin\delta\cdot\cos\delta \tag{5}$$

The normal stress can be written as:

$$\Delta\sigma_n = \Delta\sigma_Z\left(\cos^2\delta + \frac{v}{1-v}\sin^2\delta\right) \tag{6}$$

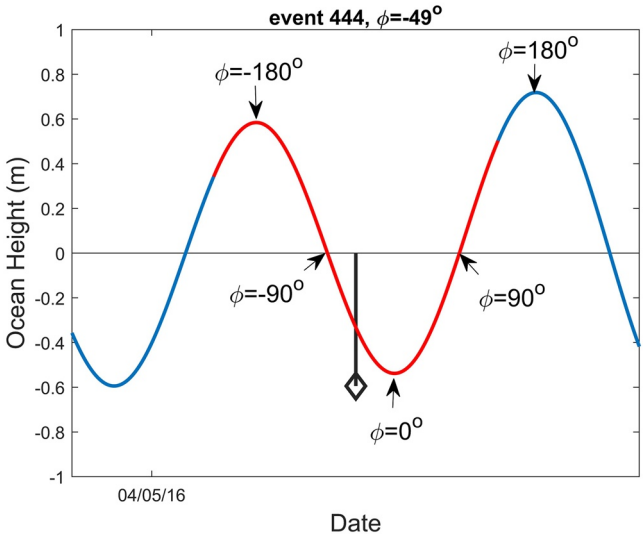

Figure 2. Example of phase, ϕ, determination. The continuous curve shows the tidal amplitude (ocean height) as a function of time, at the epicentral coordinates of the selected event, the occurrence time of which is indicated by the stem. The zero-amplitude baseline is depicted by the horizontal line. The phase count starts at minimum height, indicated as 0°. The positive phases go rightwards, corresponding to increasing ocean height (compressional stress rate), whereas negative phases go leftwards corresponding to decreasing ocean height (extensional stress rate). In the area below the baseline, where $|\phi| < 90°$ negative ocean height occurs (extensional stresses) while in the area above the baseline, with $|\phi| > 90°$ positive ocean height occurs (compressional stresses). The red curve highlights one tidal cycle centered at the event occurrence time, at −49° phase. The zero ocean height ($\sim\phi = \pm 90°$) and maximum ocean height ($\sim\phi = \pm 180°$) points are also arrow-indicated in the figure. The horizontal span is roughly 1 day.

and the difference in pore pressure, ΔP, under undrained conditions is:

$$\Delta P = -B\frac{\Delta\sigma_{jj}}{3} \quad (7)$$

where, $\Delta\sigma_{jj}$, is the stress tensor trace difference, μ is the friction coefficient and B is the equivalent for rocks of the Skempton (1954) coefficient, β, that was originally determined for soils (Rice & Cleary, 1976). We use the typical sign convention, with δ being positive downwards and λ being positive for uplift of the hanging wall (i.e., for thrust faulting). Positive ΔCFS values indicate that slip is promoted at low tides and vice versa.

Although it is expected that normal faulting prevails within the extensional regime across the ridge, it has been shown that focal mechanisms can be far more variable and complex (e.g., Parnell-Turner et al., 2017). A limited number of focal mechanism solutions for the equatorial MAR segment are available (Figure 1c), and even less for our study area (Figure 1d). In addition to computational uncertainties resulting from the network coverage, there is also uncertainty in terms of which of the two nodal planes is the fault plane. For these reasons we proceed to our analysis by taking into account tidal height and tidal phase, initially disregarding the stress calculations (e.g., Scholz et al., 2019; Wilcock, 2009). In later sections we demonstrate ΔCFS calculations for various δ, λ, μ and B combinations, effectively allowing us to determine plausible planes optimally oriented for failure at high and low tides.

For the calculations we assume $V_P/V_S = 1.74$, corresponding to a Poisson ratio $\nu \sim 0.25$. The ocean water density is set to 1030 kg/m^3, and the gravitational acceleration at the equatorial latitude is 9.781 m/s^2. A Young modulus of $E = 1.1 \cdot 10^{11}$ Pa is selected. These parameter values result in root mean square values of $\Delta\sigma_Z = 3.41$ kPa, $\Delta\sigma_Y = 0.75$ kPa and $\Delta\sigma_Y = 0.47$ kPa, showing that vertical stresses clearly prevail over the horizontal ones (Figure S2). In addition, the maximum stress rates (from high to low tide or vice versa) range between ~0.007 to 0.015 MPa/6h, corresponding to 70 and 150 cm differences in the water level, respectively, occurring during each semidiurnal tidal half-cycle. For the ΔCFS calculations, we considered $0° \le \delta \le 90°$, $0° \le \lambda \le -180°$, $0.6 \le \mu \le 0.7$, and $0.25 \le B \le 1.0$.

2.3. Tidal Phase

Given that the semidiurnal tidal period is ~12h 25', the ocean height is calculated separately, at the epicentral coordinates of each event for a time span ranging from 7h before to 7h after the event occurrence time. By doing this we ensure that a complete tidal cycle is considered and a phase within the cycle can be assigned to each event. The time step for subsequent calculations is 72 s. Since the magnitudes of solid Earth tides are secondary and they do not change abruptly in space, average values at the center of the study area are calculated for the entire study period with the same time step of 72 s.

We define the phase, ϕ, relative to the low tide, which is found to promote failure in extensional regimes (Scholz et al., 2019 and references therein). In other words, 0° corresponds to the low tide (minimum water height), ±90° correspond to zero tidal height (average water level) whereas +180° and −180° correspond to the subsequent and preceding high tides, respectively (Figure 2). Note that extensional stress (tidal height below zero) occurs at $-90° < \phi < 90°$ maximized at 0°, whereas extensional stress rate occurs at $-180° < \phi < 0°$ maximized at −90°. After defining the phase of each event, we count the number of events that occurred at specified phase bins to identify whether there is a preference for particular phase ranges.

In order to quantify the significance of the results, we perform the commonly applied Schuster (1897) test, which calculates the probability, p_s, that the occurrence times of the events, introduced as phase angles of a specified period, are randomly distributed around the unit circle. In doing so, parameter R, is defined as:

$$R^2 = \left(\sum_{i=1}^{N} \cos \phi_i\right)^2 + \left(\sum_{i=1}^{N} \sin \phi_i\right)^2 \tag{8}$$

With ϕ, being the phase angle of the ith earthquake in a population of N earthquakes. Note that the ocean tides are symmetric in the study area as verified by the symmetrical distribution of ocean tidal height values in Figure S4. Then, the probability that a given phase distribution is random is given by:

$$p_S = \mathrm{e}^{-\frac{R^2}{N}} \tag{9}$$

The lower the p_S, the higher the significance to reject the null hypothesis of random phase distribution. In other words, small p_S, indicates that there is a preference of events to concentrate near particular phase angles, implying a possible causative relationship between tides and earthquake occurrence.

2.4. Magnitude Distribution

We investigate the tidal effect on seismic sequences (i.e., temporal clusters) characterized by enhanced seismic activity, which occur at considerably higher rates than the reference seismicity. This part of analysis requires a complete catalog, since it involves seismicity rates. The Anderson-Darling (Leptokaropoulos, 2020; Marsaglia & Marsaglia, 2004) test (AD-test) is applied for different magnitude cut-off (M_{cut}) values, for verifying whether the magnitudes are drawn from an exponential distribution. The completeness magnitude is selected equal to the magnitude above which the exponentiality hypothesis is not rejected by the AD-test at 0.05 significance. Once exponentiality is verified, the b-value of the Gutenberg-Richter (GR) law is derived by the maximum likelihood estimator (MLE) of Aki (1965), together with its standard error. To quantify the significance of the b-value difference between two datasets, we apply the Utsu (1999) test, based on the Akaike Information Criterion (AIC):

$$\Delta\mathrm{AIC} = -2\left(N_1 + N_2\right) \cdot \ln\left(N_1 + N_2\right) + 2N_1 \cdot \ln\left(N_1 + \frac{N_2 b_1}{b_2}\right) + 2N_2 \cdot \ln\left(N_2 + \frac{N_1 b_2}{b_1}\right) - 2 \tag{10}$$

where N_1, N_2 are the number of events and b_1, b_2 the corresponding b-values of the two datasets, respectively. The Utsu test gives the probability, p_u, that two given datasets are drawn from the same population (same b-values), defined as:

$$p_u = e^{-\left(\frac{\Delta\mathrm{AIC}}{2} - 2\right)} \tag{11}$$

The lower the p_u, the stronger the indication that the b-values of the two datasets differ. Finally, to evaluate seismic potential as the combined effect of seismicity rates and magnitude distribution, we characterize the difference in seismicity between high and low tides in terms of hazard parameters. In particular, the exceedance probability (EP) of a predefined magnitude (M_t) within a fixed time period (T_t) is calculated as:

$$\mathrm{EP} = 1 - e^{-rT_t\left(1 - F_m\left(M_t\right)\right)} \tag{12}$$

where, r, is the seismic activity rate above M_C and F_m, is the magnitude Cumulative Distribution Function. Since the AD-test verifies the exponentiality of magnitude distribution in all cases with $M_{cut} \geq M_C$, we calculate F_m considering the unbounded GR law as:

$$F_m = 1 - e^{-b\left(M - M_C + \frac{\Delta M}{2}\right)}, \; for\; M \geq M_C, 0, \mathrm{otherwise} \tag{13}$$

with ΔM, being the magnitude round-off interval of the catalog. The EP calculations and their bootstrap confidence intervals (CI) are performed using the SHAPE toolbox (Leptokaropoulos & Lasocki, 2020).

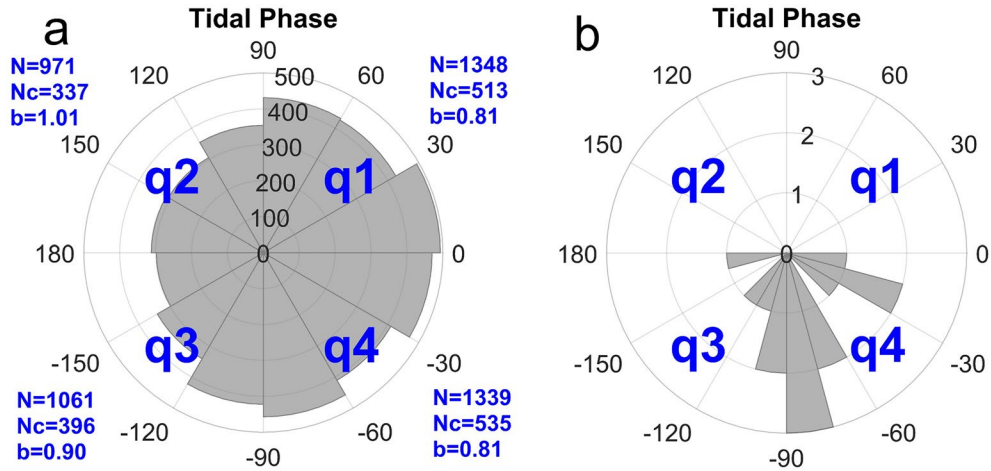

Figure 3. Polar histograms of tidal phases for (a) the entire data of 4,719 events and (b) the initiation of the 14 enhanced activity rate clusters (see main text for description). The numbers at the outer circles indicate the phase in degrees, while the concentric circles show the number of events. The blue fonts in (a) represent the number of events (N), the number of events above completeness magnitude, $M_C = 0.01$ (Nc) and the corresponding b-value in each quadrant (q_1-q_4), starting from upper right corner, counter-clockwise.

3. Results

3.1. Statistical Analysis of Seismicity Rates and Magnitudes Within the Tidal Cycle

We first search for potential correlation between event occurrence times and ocean tide phases, ϕ. Figure 3a shows the distribution of phases for the entire data set of 4,719 events. The Schuster test verifies that there is a preference for particular phase angles at a very high significance ($p_S \sim 10^{-25}$). There is a visible preference of event occurrence at low tides ($-90° < \phi < 90°$) with the most populated bins corresponding to $-30° < \phi < 30°$. Moreover, the binomial test suggests that the difference between the number of events that occurred at low tides (~57%) and those that occurred at high tides (~43%) is significant with $p \sim 10^{-21}$. We further investigate the magnitude dependence of the tidal triggering, considering diverse magnitude classes shown in Table 1. As the magnitude threshold increases, higher fractions of seismicity tend to occur at low tides (57%–69%), suggesting that stronger events are more prone to tidal triggering. Although the p-value derived from the binomial test declines in each case due to the decreasing sample size, it remains below 0.05 for all cases tested. Following Cochran et al. (2004), the percentage of the excess events, N_{ex}, is defined as $N_{ex} = 100N_{enc} - N_{tot}/2/N_{tot}$, where N_{enc} is the number of events occurring at encouraging ocean tidal height (stress), and N_{tot} is the number of total events. In our data set $N_{ex} = 7\%$ (2,687 out of 4,719 events) and gradually increases for higher magnitude thresholds (Table 1). These values for our study area are considerably higher than the ones obtained in other studies (e.g., Cochran et al., 2004; Wilcock, 2009) for datasets of comparable sizes. Regarding results from other MOR spreading centers, in particular the East Pacific Rise at 9°50'N, Bhatnagar et al. (2015) report N_{ex} up to 9%, Stroup et al. (2007) estimated $4\% < N_{ex} < 19\%$, whereas Tan et al. (2018) found N_{ex} values as high as 20%.

Table 1
Statistical Properties of the Earthquakes Distribution That Occurred at Low Tides ($|\phi| < 90°$)

	N with $\lvert\phi\rvert < 90°$	% of total	p-value binomial	N_{ex}
All data	2,687	56.9%	10^{-21}	6.94% ± 0.72
$M > 0.0$	1,048	58.8%	10^{-13}	8.84% ± 1.17
$M > 1.0$	152	61.8%	0.0001	11.79% ± 3.10
$M > 1.5$	69	70.4%	0.0003	20.41% ± 4.61
$M > 2.0$	25	69.4%	0.0144	19.44% ± 7.68
$M > 2.5$	12	75.0%	0.0384	25.0% ± 10.83

Note. The first column shows the magnitude cut-off value. The second and third columns show the number of events that occurred at low tides and their percentage to the total data, respectively. The fourth column presents the p-value of the binomial test and the fifth column shows the excess events, N_{ex}, percentage and the corresponding standard deviation (Cochran et al., 2004).

The lowest number of events as well as the highest b-value are found at the quadrant q_2 ($90° < \phi < 180°$ see Figure 3a) which corresponds to high compressional stress and compressive stress rate. Quadrant q_3, corresponding to compressional stress but extensional stress rate, demonstrates a slightly lower b-value and higher event numbers. Finally, quadrants q_1 and q_4, which correspond to extensional stresses, exhibit almost identical numbers of events and b-values. The event numbers in q_1 and

Table 2
Properties of the 14 Enhanced Activity Rate (EAR) Clusters Identified in the Study, Shown in Figure 4

Cl.	N	T_{cl} (min)	r (events/h)	M_1	M_{max}	M_{max} rank	ΔM	Phase (°)
1	25	52	28.80	2.29	2.97	12/25	0.68	−84.1
2	12	120	6.00	0.38	0.73	3/12	0.10	−30.0
3	17	24	42.50	0.12	1.93	6/17	0.53	−91.6
4	12	51	14.12	2.60	2.60	1/12	1.21	−68.8
5	12	70	10.29	3.42	3.42	1/12	2.16	−106.3
6	24	104	13.85	1.47	2.41	5/24	0.10	−97.1
7	10	71	8.45	0.22	1.20	5/10	0.31	−28.3
8	33	144	13.33	1.87	2.76	28/33	0.89	−134.1
9	42	203	12.30	0.15	2.13	14/42	0.21	−65.0
10	12	92	7.83	1.25	2.23	7/12	0.98	−84.4
11	47	169	21.77	1.22	4.00	2/47	2.08	−22.0
12	14	71	13.00	2.82	2.82	1/14	0.95	−165.3
13	22	98	17.65	0.20	2.27	12/22	0.23	−84.9
14	19	130	8.77	0.19	2.84	17/19	1.65	−13.9
Sum:	301	23.3 h				*Mean:*		**−82**

Note. The first column depicts the cluster ID (in chronological order). "N", shows the number of events comprizing each cluster. "T_{cl}", shows the duration of the cluster, whereas "r", indicates the corresponding activity rate. M_1, shows the magnitude of the first event of each cluster. "M_{max}" and "M_{max} rank", depict the magnitude of the strongest event and its rank within each cluster (i.e., the position of the strongest event within the sequence), respectively. "ΔM", shows the magnitude difference between the two strongest events in each EAR cluster. "Phase" demonstrates the phase corresponding to the first event of each EAR cluster (beginning of the sequence). The last row indicates the sum for "N" and "T_{cl}" and the mean value for "Phase."

q_4 are higher than in the other two quadrants, whereas the b-values are 0.1 and 0.2 units lower that the corresponding values observed in q_3 and q_2, respectively. The cumulative magnitude distribution of events within quadrants q_1-q_4 are shown in Figure S5a.

Similar results are derived when considering event occurrences versus tidal height. We define the background sample as all the tidal height values calculated for the area during the study period (~1 year), with the applied time step of 72 s. The relative frequency of this background sample is strongly symmetric with roughly the same number of observations occurring at both low and high tides (Figure S4). However, this symmetry breaks when the tidal height values corresponding to the occurrence times of our seismic catalog events are considered. There is an excess of events that occur during negative heights (low tide) and an event deficit at high tides, in comparison with the background population of tidal height fluctuation. This clearly indicates a preference of earthquake occurrence on our study area at low tides.

The next step is to determine whether tides trigger seismicity with enhanced activity rates (EAR), in the sense of temporal clusters, that is, sequences occurring at much higher rate than the overall seismic activity (Figure 3b). Note that we use the term "cluster" to refer to small interevent times and not dependence/triggering among the events. For that purpose, we first filter the catalog to include only data above completeness magnitude, M_C, which is found equal to 0.01 (Figure S6). In order to seek for potential spatial incompleteness, we study the magnitude distribution of the four most populated template-based event families and find that their M_C ranges between −0.70 and −0.24. The most populated family, having 1,333 events, is also one of the most distant from station L33D (3 km). Yet, the M_C was found to equal −0.25. If we further consider the 517 events located at greater distances (i.e., distances 3.0 km < D < 4.8 km), the corresponding M_C is estimated to equal −0.17. Thus, the 0.01 selection for the entire data set should be a reasonable choice, ensuring catalog completeness at high confidence. We should stress, however, that our catalog doesn't likely represent all the types of seismicity that occurred on the ridge during the deployment period—that is, our catalog is by no means complete along the entire ridge segment. However, it should be true that our catalog is complete for the event families that are represented by the templates—so any magnitude of completeness values quoted should be caveated with this.

We define such EAR clusters as sequences containing at least 10 events with a time difference between subsequent events less than 30 min. In this way EAR clusters contain a sufficient number of events to discriminate from occasionally random, clustered occurrences. The results (Table 2) also show that the duration of the identified clusters remains well below the semi-diurnal tidal half-period of ~6h, to unequivocally locate each EAR cluster at a particular phase. Fourteen such clusters are identified. Note that the mean rate for the events above $M_C = 0.01$ is ~0.22 events/h, whereas the EAR clusters exhibit seismicity rates from 6 to over 40 events/h, that is, from ~25 to ~200 times higher rates.

Both Table 2 and Figure 4, show that all of the 14 EAR clusters identified, exclusively initiated (first event occurrence time) at negative tidal phase, with a particular preference close to high extensional stress rates (ϕ close to −90°). Twelve out of 14 cluster initiation times (Figure 3b) are located within an ~90° range (from −106° to −14°) in the phase of the tide. The Schuster test $p_s = 0.0003$, verifies that EAR clusters predominantly initiate at a specific phase range. In addition, the phase of all 301 clustered events lies between −165° and 59°. These events correspond to 22 out of the 34 templates and are mainly distributed along or close to the ridge axis, with most events located ~2 km north of station L33D (See Figure S7a). Furthermore, 80% of the clustered events occurred at −100°< ϕ < 15°. If we consider the combined influence of the ocean

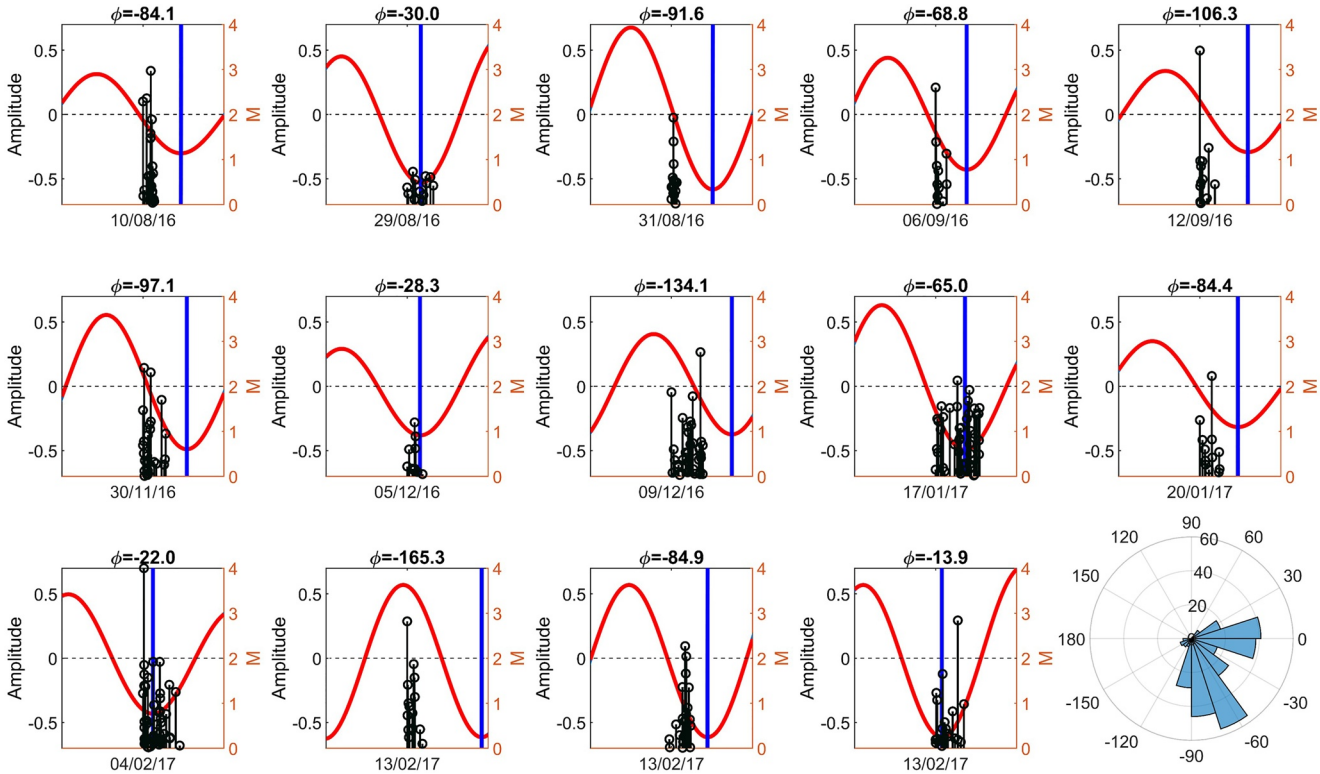

Figure 4. Comparison of the 14 enhanced activity rates (EAR) clusters with the tidal cycle. Tidal cycle is indicated by the red curve, centered at the occurrence time of the first event of each EAR cluster, the tidal phase of which is written on the top of each panel. Stem plots show occurrence time of the events within each cluster, with the right *y*-axis indicating their magnitude. The blue vertical line depicts the minimum ocean height, corresponding to $\phi = 0°$. The dashed horizontal line shows the reference ocean level (zero height). The time span on the *x*-axis is roughly 12h. Note that the last three sequences occurred at the same day. The polar histogram at the lower right corner shows the tidal phases of all the 301 events comprising the 14 EAR clusters.

tides and solid Earth tides, the phase of the stress is shifted by up to ~40° counter-clockwise at a few times during the year. However, there is only a slight overall change in the phase of the EAR clusters (Figure S8) and the corresponding p_s values are identical. We should, however, point out, that both Schuster and binomial tests performed under the assumption of independent earthquakes occurrence may not be completely valid for our data set. Although there is a clear and strong tidal signal in the seismicity data, the significance of both statistical tests may be overestimated for individual earthquakes (Figure 3a, $p_S \sim 10^{-25}$) if there is any triggering (e.g., earthquake interactions, magma chamber influence). However, the tests should be more realistic when calculated for the clusters of events (Figure 3b, $p_S \sim 0.0003$).

The event magnitude distribution is then investigated. The complete data set is comprised of 1,781 events ($M \geq 0.01$) with a MLE b-value equal to $b = 0.83 \pm 0.02$. We search for a difference in magnitude distribution between events that occurred during low tides ($|\phi| < 90°$) and high tides ($|\phi| > 90°$). One thousand and forty eight events occurred at low tides with a MLE $b = 0.81 \pm 0.03$, whereas 733 events occurred during high tides with MLE $b = 0.85 \pm 0.03$. Although the two b-values are similar, a closer look at the entire magnitude distribution reveals significant deviations between the two datasets (Figure S9). During low tides the b-value is rather stable around 0.80, while during high tides the b-value fluctuations are remarkably wider, ranging between 0.85 and 1.00. In addition, for $0.25 < M_{cut} < 0.45$, the magnitudes at high tides fail to pass the AD test at 0.05 significance, indicating a considerable deviation from GR law. This suggest that either a different physical process leads to such deviation from exponentiality, or that mixed data with diverse properties comprise the high-tide data set.

Previously we established that the number of events at low tide is higher (Figures 3 and 4); however visual inspection of Figure 3a suggests that there is an even greater discrepancy if we divide the events slightly differently than just by low ($|\phi| < 90°$) versus high ($|\phi| > 90°$) tide. For instance if we rotate the division by 45° clockwise and divide the sample at $-135° < \phi < 45°$ for Group 1 and $45° < \phi < 180°$ and $-180° < \phi < -135°$

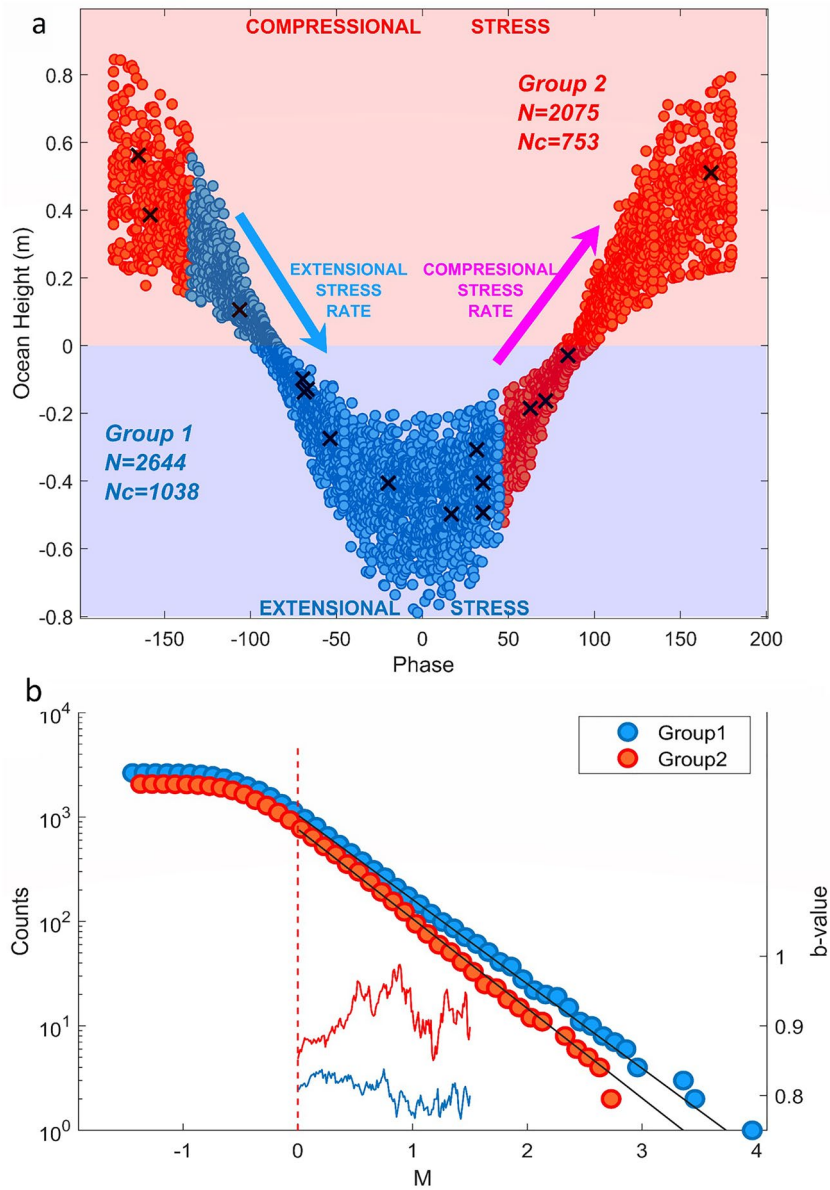

Figure 5. Group 1 and Group 2 events in a ocean height-phase plot and their corresponding magnitude distributions (a) Ocean height plotted against phase (circles). Red-shaded surface indicates positive ocean height, corresponding to compressional stresses. Blue-shaded surface shows negative ocean height, corresponding to extensional stresses. The blue descending arrow and pink ascending arrow depict the domains of maximum extensional and maximum compressional stress rates, respectively. The total number of events (N) and the number of events with $M_L \geq 0.01$ (Nc) is also indicated for each group with the respective colors. The black crosses show the strongest events with $M_L \geq 2.5$ Blue circles represent Group 1, that is, events occurred during either high extensional stress or high extensional stress rate. Red circles represent Group 2, that is, events that occurred during either high compressional stress or high compressional stress rate. (b) Magnitude-frequency distribution (cumulative) for Group 1 (blue circles) and Group 2 (red circles). The blue and red curves indicate the corresponding b-values for different magnitude cut-off values from 0.01 (equal to Mc) to 1.50. The vertical red dashed line depicts the $M_C = 0.01$. The straight black lines show the MLE fit for $b = 0.809$ (Group1) and $b = 0.859$ (Group 2).

for Group 2 (Figure 5a). In such way, we apply a more flexible approach, allowing a time lag of the tidal response to apply. Group 1 thus includes events that occurred during both maximum extensional stress ($\phi = 0°$) and maximum extensional stress rate ($\phi = -90°$). In the same way, Group 2 includes events that occurred during both maximum compressional stress ($\phi = \pm 180°$) and maximum compressional stress rate

($\phi = 90°$). Group 1 (1,038 events above Mc = 0.01) exhibits considerably higher activity rates than Group 2 (753 events above Mc = 0.01). The magnitude distribution of the two groups is shown in Figure 5b. Group 1 demonstrates $b = 0.81 \pm 0.025$, whereas Group 2 has $b = 0.86 \pm 0.032$. The AIC returns $p = 0.17$, suggesting that the difference between these values cannot be considered as significant. The plot of b-values as a function of magnitude cut-off (Figure 5b) indicates a dependence of b-value on magnitude cut-off, especially for Group 2. Note that the AD-test for exponentiality is not rejected at any magnitude cut-off for neither Group 1 nor Group 2, in contrast to considering events that occur at low/high tides (Figure S9). The magnitude distribution of the 4 quadrants shown in Figure 3, after being shifted by 45° are shown in Figure S5b. To summarize, both division approaches (high-low tides and Group 1-Group 2) lead to similar results as far as the number of events and magnitude distribution are concerned. This verifies a clear preference of events occurrence close to 0° compared to 180°, even if a short time lag is evident.

We further assess the tidal effect on seismic potential in terms of combined activity rate and magnitude distribution. In doing so, we calculate exceedance probabilities for specified magnitudes during a predefined time-period. Activity rates are considered to be equal to the corresponding number of events divided by half the duration of the entire data set, since the whole period of study comprises an almost complete sequence of tidal cycles. In Equation 12 we set, $T_t = 365$ days, and we obtain $EP_{Group1} = 0.185$ (95% CI: 0.111–0.309) and $EP_{Group2} = 0.108$ (95% CI: 0.057–0.208) for $M \geq 5.0$ and $EP_{Group1} = 0.031$ (95% CI: 0.017–0.064) and $EP_{Group2} = 0.016$ (95% CI: 0.007–0.036) for $M \geq 6.0$. Exceedance probabilities are almost twice as large for Group 1, suggesting that seismic potential is higher both during low tides and approaching low tides, resulting as a combination of higher activity rates and more frequent large events within the respective magnitude distribution. However, the 95% CIs exhibit a considerable overlap in both cases.

Finally, we compare the aggregated magnitude distribution of the EAR clusters, containing 301 events with the remaining, non-clustered seismicity. The result is that EAR clusters demonstrate a MLE $b = 0.61 \pm 0.04$ whereas the remaining data above M_C, contain 1,480 events with MLE $b = 0.89 \pm 0.02$. These b-values statistically differ from each other at very high confidence, according to the AIC, demonstrating $p_u < 10^{-7}$. This shows that enhanced seismic activity with considerably higher seismic potential in terms of both activity rates and magnitude distribution is exclusively triggered during either high extensional stress, or high extensional stress rates (i.e., at roughly $-120° < \phi < 30°$, Figure 3a). Note that this result is different from the more common observation that clustered seismicity (e.g., swarms) especially in volcanic and geothermal areas usually demonstrate high b-values (e.g., El-Isa & Eaton, 2014). However, the clustered activity we present here corresponds to a very small timescale of a few hours, therefore it cannot be directly associated with the general characteristics of swarms.

3.2. Effect of Tidal Coulomb Stress on a Range of Fault Planes

Up to this point, we only considered the effect of tidal height and polarity, on seismicity. Here we focus on the tidally induced Coulomb stress changes on various fault plane geometries and parameter values. A commonly applied practice is to use a modified version of Equation 4, as

$$\Delta CFS = \Delta\tau + \mu'\left(\Delta\sigma_n\right) \tag{14}$$

where μ' is the apparent friction coefficient incorporating pore fluid effects and temporal changes of the effective normal stress (e.g., Linker & Dieterich, 1992). However, this approach is a simplification in an attempt to counterbalance our lack of knowledge regarding the role of pore fluids. The apparent friction coefficient may be written as (Simpson & Reasenberg, 1994):

$$\mu' = \mu\left(1 - B\right) \tag{15}$$

with B, experimentally determined to take values from 0.47 to 1.0 (Harris, 1998 and references therein), corresponding to a gradual transition from drained to fluid-saturated conditions, respectively. Figure 6 shows the ΔCFS derived by application of Equations 4–7 for a variety of fault plane orientations and parameter values. Note that this approach leads to a somewhat different ΔCFS pattern than the one derived by simply setting a μ' value (Equation 14, Figure S10).

Informed choices must be made about the fluid pressure and coefficient of friction for Coulomb stress calculation, which in turn affect the fault dip and rakes that are predicted to promote slip. In terms of fluid

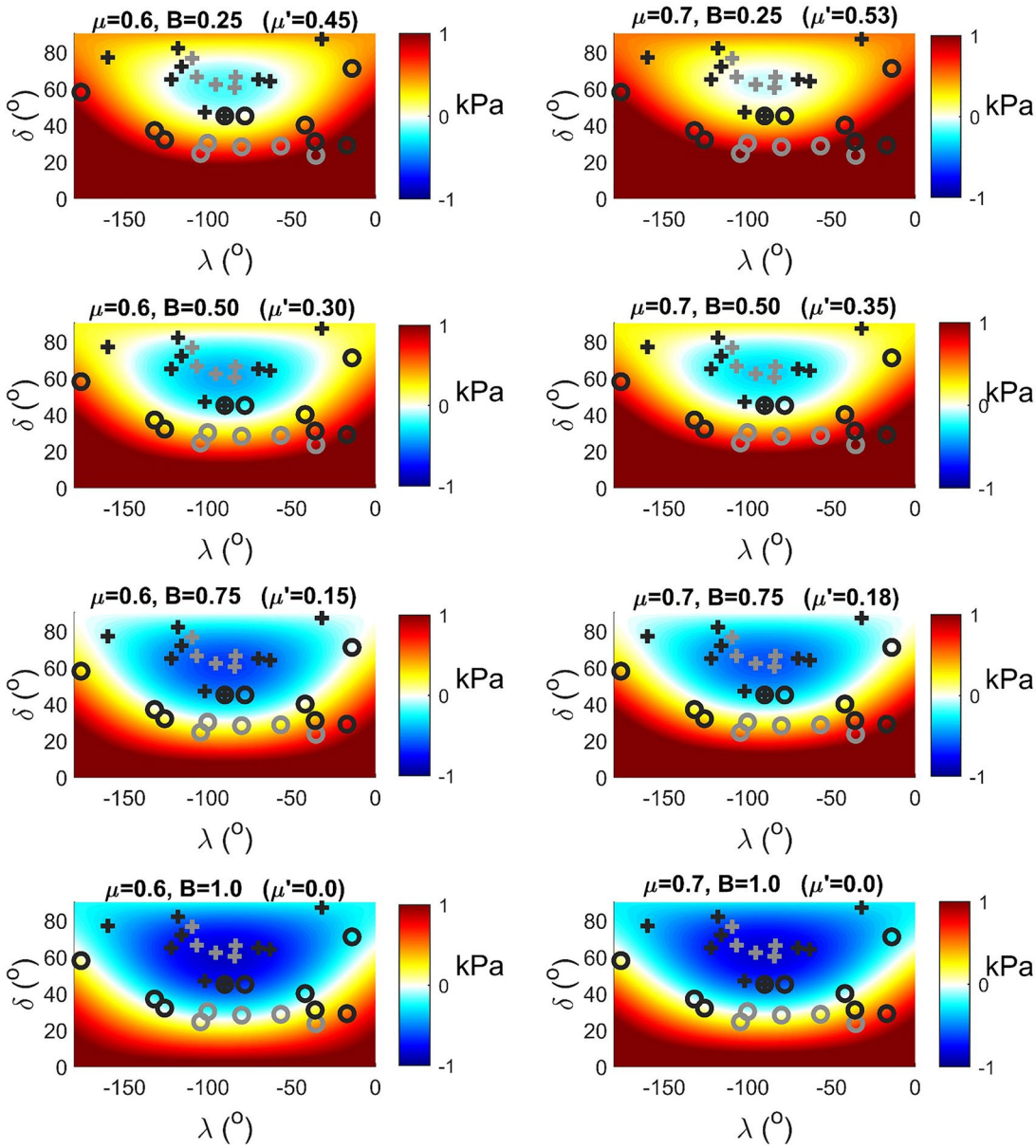

Figure 6. Tidal ΔCFS for dip (*y*-axis) ranging between 0° and 90° and rake (*x*-axis) ranging between −180° and 0°. Each frame corresponds to different values of friction coefficient, μ, and Skempton coefficient, B, (the number in parenthesis denotes the resulting apparent friction coefficient, μ', estimated from Equation 15). The warm colors indicate positive ΔCFS (slip is promoted by low tides), while cool colors indicate negative ΔCFS (slip is inhibited by low tides). The calculated values correspond to a tidal height of −70 cm. The available focal mechanisms are also depicted in the plot. Circles correspond to the shallow-dipping planes (<45°) while crosses indicate the steep-dipping planes (>45°). Black and gray marks correspond to the solutions obtained by GCMT and this study, respectively. The color scale has been saturated at 1 kPa for clarity.

pressures, Scholz et al. (2019) state that the lack of a time lag between tidal stress and seismicity occurrence indicates undrained conditions. The best division of our events included a 45° rotation, which may indicate a time lag. This suggests some amount of draining may be occurring. Tesei et al. (2018) compiled a table of friction coefficients, μ, for different temperatures and effective normal stresses, showing a wide range for serpentinites between 0.1 and 0.8, with dry samples usually characterized by $0.5 < \mu < 0.8$ and saturated samples of lizardite and chrysolite being mostly within the range $0.1 < \mu < 0.4$. For a reasonable choice of Skempton coefficient for unsaturated conditions (0.50–0.80, e.g., Harris, 1998), the apparent friction coefficient values lie within the range $0.1 < \mu' < 0.4$. Therefore, although for $\mu' > \sim 0.5$ (Figures 6 and S10,

Wilcock, 2009) failure is promoted at virtually all possible fault planes during low tides, previous research suggests that the apparent friction coefficient values may instead be sufficiently lower.

We test the available focal mechanism solution geometries against various friction values. There are five focal mechanisms available for our data set, two of them indicating normal faulting and the remaining three demonstrating a dominant strike-slip component (Figure 1d). However, these solutions have considerable uncertainties, particularly in the fault dip angle due to the insufficient network coverage. For this reason we further used the available focal mechanisms from the entire ridge segment (Figure 1c). There are 12 focal mechanisms obtained from the OBS recordings, which are fairly similar to each other. On average, they delineate two fault planes, one with $\delta = 63°$ and $\lambda = -97°$, and a second plane with $\delta = 30°$ and $\lambda = -75°$. The first plane, requires a $\mu' > 0.57$ in order to promote failure at low tides, while the second, shallow-dipping plane requires a $\mu' > 0.34$ to favor slip during low tides. Results are similar for the 21 focal mechanisms obtained from Harvard Global Centroid Moment Tensor (GCMT), requiring $\mu' > \sim 0.57$ and $\mu' > \sim 0.43$ for the steep-dipping and the shallow-dipping planes, respectively (Figure 6).

4. Discussion

The Coulomb stress modeling suggests that either slip is triggered on a low angle, low friction fault or that friction is high, in which case slip could be triggered on faults at almost any angle, including high angles. High angle faults require μ' values higher than 0.5 or 0.6, which would suggest drained conditions with B being well below 0.5. This is within the range of reasonable estimates given our previously discussed observation of time lag between the tide and seismicity, suggestive of partially drained conditions (Scholz et al., 2019). However, high μ' values are consistent with strong lithosphere, which may not necessarily be the case beneath the oceans.

There are several lines of geological evidence that support weak, low friction faults in the oceanic crust and mantle. Evidence from the ocean drilling program suggests that there is often extensive high and low temperature alteration within fault zones in the oceanic crust, with fractures often containing minerals assemblages including clays and micas that would tend to lower the coefficient of friction on faults and fractures (Früh-Green et al., 1996). Low coefficients of friction in the crust would favor slip at low angles (20°–40°), associated with detachments faults or the listric base of the high angle faults visible in the nearby seafloor topography (Figure 1d). This low friction is needed to explain detachment faults in general (Cann et al., 1997). In addition, some of the deepest earthquakes may be in the uppermost mantle. Although oceanic crust is on average 6–7 km thick, and shows little variability especially beneath the Pacific (Bown & White, 1994; Christeson et al., 2019), Atlantic crust is more variable in thickness than Pacific crust (Cannat, 1996; Dunn et al., 2017). Specifically, one nearby seismic refraction study suggests the crustal thickness varies between 4.8 and 6.25 km on the western flank the ridge segment (Marjanović et al., 2020), with a similar thickness (4–6 km) from S-to-P receiver function imaging in the study area (Rychert et al., 2021). Oceanic mantle lithosphere is typically assumed to be weak given the abundant presence of lizardite and chrysolite serpentinites in the mantle (e.g., Escartin et al., 1997; Tesei et al., 2018). Escartin et al. (2001) showed that even a small degree of serpentinization (<15%) can reduce the oceanic strength to that of pure oceanic serpentinite, near the ridge axis. So, triggering along high angle extensional faults is less likely. Further weakening may also occur due to increased pore fluid pressures and strain localization caused by the low internal friction of altered oceanic lithospheric rocks.

Additional information about whether high-friction, high-angle faults are tidally triggered can be gathered by the seafloor morphology and depth distribution of seismic hypocenters and their relationship to the triggered clusters. High angle westward dipping fault scarps are visible in the high resolution bathymetry of the region (Figure 1b), and this is consistent with horst and graben type structure that creates abyssal hill fabric. This morphology suggests there has to be high angle faults at shallow depths, in contrast to other locations in the region which show hummocky detachment fault morphology (Harmon et al., 2018). Although the well-constrained relocated data consists of only 34 events, Figure 1d shows that the hypocenters delineate a west-dipping structure, starting with a relatively high angle (>45°) at shallow depths (<8 km). The shallowest focal mechanism has a westward dip ~57° (Figure 1d). For the deeper segments, however, the earthquake distribution does not provide unequivocal conclusions. The fault may either continue to the

deeper segments at a relatively high angle (e.g., line A-A1, Figure 1d) or rotate to a lower angle, forming a listric structure (e.g., line A-A2, Figure 1d). Regardless, both options appear relatively listric in structure. In addition, the tidally triggered clusters occur along the ridge axis (Figure S7), in other words within the lower angle sections of the listric faults, rather than the more steeply dipping sections off-axis (Figure 1d). It seems therefore, very plausible, that the lower part of the listric fault ends in weak, serpentinized mantle whereas the upper fault segment is located in the basaltic oceanic crust and is therefore, stronger.

Another possibility is that triggered slip may be promoted at low tides after incorporating the influence of a magma chamber. In other words, the magma chamber could inflate owing to its higher compressibility, potentially resulting in a favorable stress field, as has previously been proposed for a fast spreading ridge (Scholz et al., 2019). Deeper strike-slip events, with non-double couple components could be consistent with related dyking events (e.g., Minson et al., 2007). Magma chambers have rarely been imaged at slow spreading ridges like MAR, and it is often assumed that there is insufficient melt production to create an axial magma chamber. The most prominent example is the presence of a crustal magma chamber beneath the Lucky Strike segment of the MAR (Singh et al., 2006). Yet, local Rayleigh wave imaging found slow velocities in the upper 20 km depth beneath the ridge segment studied here (Figure 1), slower in comparison to the segment just to the south of Chain Fracture Zone, interpreted as the existence of upwelling mantle and/or increased melt fraction (Saikia et al., 2021). Therefore, there is ongoing evidence that such magma chambers exist at slow-spreading ridges, and in particular possibly this spreading center, and thus mechanisms proposed for fast-spreading ridges may, at least sometimes, apply in slow-spreading ridges as well. In addition, in our data set, the events having the strongest connection to low tides are associated with the most populated template events, parallel to the ridge axis (Figure S7b). The rest of the events demonstrate a weaker correlation and the northernmost cluster exhibits a strong preference for occurrence times during high tides. This may further support the existence of a magmatic body beneath the ridge, which causes a localized effect.

Our observations of lower b-values at high extensional stresses agree with previous results from Axial Seamount (Tan et al., 2019), although we also found lower b-values for high extensional stress rates. Tan et al. (2019) analyzed the magnitude frequency distribution of >20,000 microearthquakes within a 25 km^3 block of crust at Axial Seamount, which is subject to tidal loading of ±20 kPa. They showed that b-values are inversely correlated with Coulomb stress, varying by ~0.09 per kPa. We could not establish a similarly robust relation in our data set, which has over 10 times less data (1,781 events above M_C). Nevertheless, we detect anomalous deviations from GR law during high tides ($|\phi|>90°$), with the b-value varying in a way that cannot be attributed to random fluctuations or an insufficient sample. Moreover, during high tides, for a 0.2 magnitude unit range, the AD test rejects the exponentiality hypothesis at 0.05 significance (Figure S9). We perform the Schuster test to seek for detection bias during the hours of the day. There is no significant preference at particular hours ($p_s = 0.20$), something that is rather expected in an oceanic environment in the absence of anthropogenic noise, predominantly present during daytime in continental areas. Note, however, that the fact that detection level may be correlated with the tides cannot be ruled out (e.g., Hilmo & Wilcock, 2020). Nevertheless, we estimated that M_C fluctuated between −0.34 to −0.05 during different tidal phase ranges. Therefore, the selected Mc = 0.01 most plausibly secures completeness in our data set. Thus, excluding the explanation that the detection level of the network decreases at high tides, our results indicate that either a periodic, tidal-induced deviation from GR law occurs at high tides, or that the selected data set is, to some large degree, inhomogeneous. Further analysis showed that division of events at a slightly different tidal phase (e.g., Group 1 and Group 2, Figure 5) leads to datasets following exponential distribution, but also demonstrating considerable b-value fluctuations. Overall, our analysis suggests that higher seismicity rates and lower b-values occur at high extensional stresses in agreement with Tan et al. (2019), but also at high extensional stress rates.

There are some limitations in our catalog that need to be stressed, in particular regarding the magnitudes. The large and wide ranging inter-station spacing of the PI-LAB network (from 30 to >200 km) makes it difficult to use a network template-matching approach for our study area. Moreover, the signals from the mostly small events beneath the ridge are quite strongly attenuated. It is thus difficult for them to be seen on multiple stations. It would be very difficult and less reliable to obtain a more complete and well-located catalog of templates based on events which were large enough to be detected through more conventional

means (arrival time association and waveform back-projection) with multiple stations. Our approach does not pose a major problem for our study purposes since we are mainly investigating the temporal distribution of certain clusters. There is, however, an impact on the magnitude for the catalog events, which is evaluated from only one station, inherently leading to uncertainties. It is also unknown how M_L scales with M_w. This means that our b-values can be used to compare the properties of different datasets in our study area; however, they cannot be compared to other studies due to their strictly local character. Additional uncertainties arise from the relatively small sample size (<1,800 events with $M \geq M_c$), which decreases to some hundred events in particular subsets considered in our analysis, that is, in specified phase ranges. The limited data size results in uncertainties in both b-value and exceedance probability estimation. Therefore, statistical significance (e.g., 0.05) could not be achieved. Moreover, although the AD test cannot reject the exponentiality hypothesis in all the datasets we tested, with one exception (Figure S9), there is a strong dependence of b-value on magnitude cut-off selection. This means that, although unlikely, the GR law violation and/or the temporal catalog incompleteness cannot be unequivocally ruled out (e.g., Herrmann & Marzocchi, 2020; Leptokaropoulos et al., 2018; van der Elst, 2021). However, even without achieving a strong statistical significance, the derived results indicate some relative differences in the magnitude distribution of events during different stages of tidal cycles, suggesting further investigation of larger datasets with better determined magnitudes is warranted.

Some very interesting conclusions also become apparent as we quantify the tidal effect in terms of seismic potential, incorporating the influence of both seismicity rates and magnitude distribution. We argue that larger magnitude events (e.g., $M \geq 5.0$ or $M \geq 6.0$) are more likely to occur during, or just before low tides rather than during or towards high tides. This is, however, a speculation given that our data set is limited to events with $M_L < 4.0$. Tanaka et al. (2002) found a significant correlation between global, strong ($M > 6.0$) shallow, normal fault type events and the stress tensor trace. Our preliminary results across MAR cannot verify any such significant correlation, suggesting that this effect is either weaker in the entire Atlantic Ocean or highly localized. Ide et al. (2016), proposed that small tidal stresses can accelerate slow deformation at various scales, and the resultant stress redistribution may increase the cascading probability of nearly critical dynamic rupture, that is, the probability of an event's transition from small to large scales. Such potential is clearly evident in our study, as verified by the EAR cluster analysis. The 14 EAR clusters identified have a total duration of ~1 day however, they accommodate 38.5% of the $M \geq 2.0$ events (including the 2 strongest earthquakes), or equivalently, 83% of the total seismic moment release. Figure 3b shows that EAR clusters are much more likely to initiate during or close to maximum extensional stress rate, suggesting a significant role of stress rate in initiating cascades of events, which continue as far as favorable conditions (extensional stresses) apply. This is also evident in the entire data set, when the highest seismic activity rate is found not only during high extensional stresses ($-30° < \phi < 30°$, Figure 3a), but also during high extensional stress rates ($-120° < \phi < -60°$, Figure 3a). Plausible mechanisms include the decrease in confining pressure at low tides which in turn leads to a decrease in normal stress, causing slip on mature faults (e.g., Tolstoy et al., 2002) and the tidal perturbation of fluid pressure within the cracks, caused by the overburden water load fluctuation (Stroup et al., 2009; Tolstoy et al., 2002). A time-dependent component of diffusive pore pressure perturbations is a plausible mechanism to explain the observed phase lags between tidal loading and earthquake occurrence (Fang et al., 1993; Stroup et al., 2009).

5. Conclusions

We investigated the possibility of tidal triggering of microseismicity in a small volume of oceanic lithosphere at an equatorial MAR segment from ~1-year of data. Our major finding is that the occurrence of events during and towards low tides prevails within the total activity and exhibits high statistical significance. The results are summarized as follows:

1. Two groups of events can be distinguished: Group 1 comprises events that occurred during either high extensional stress or high extensional stress rates (i.e., during and towards low tides). Group 2 comprises events occurred during either high compressional stress or high compressional stress rates (i.e., during and towards high tides). Group 1 is characterized by higher activity rates and smaller b-values in comparison to Group 2.

2. Twelve out of the 14 EAR clusters (seismicity bursts at remarkably high rates), belong to Group 1. All EAR clusters initiated at extensional stress rates and half of them occur very close to the maximum extensional stress rate.
3. Exceedance probabilities of strong events ($M > 5.0$) are considerably higher in Group 1 (EP = 0.19, $r = 6.2$ events/day, $b = 0.81$), than in Group 2 (EP = 0.11, $r = 4.2$ events/day, $b = 0.86$).
4. Coulomb stress modeling is consistent with tidal triggering on low-angle normal faulting in a serpentinized, low-friction oceanic lithosphere.
5. Coulomb stress modeling in combination with the apparent fault plane from morphology and earthquake locations, the assumption of serpentinization at shallowest depths and also strike-slip focal mechanisms suggest additional factors such as the influence of an underlying magma chamber may be required to explain the tidal triggering on high angle faults, at low tides.

Data Availability Statement

The seismic data are archived at the IRIS DMC, as 2016–2017 network XS https://doi.org/10.7914/SN/XS_2016 (Rychert et al., 2016). The global seismicity data come from Teza et al. (2016) (data available at http://geophysics.geo.auth.gr/ss/CATALOGS/Catalog_MidAtlantic_1904-2014.txt, last accessed June 2021). The earthquake catalogue compiled and used in the study is available in the Data Set S1. Some of the moment tensors come from www.globalcmt.org/, last accessed March 2021. Figure 1 was generated using Generic Mapping Tools v.6.1.1 (www.soest.hawaii.edu/gmt, last accessed March 2021). The codes for Anderson-Darling test and the SHAPE toolbox for hazard parameters estimation can be downloaded from https://git.plgrid.pl/projects/EA/repos/sera-applications/browse/, last accessed March 2021.

Acknowledgments
C.A. Rychert, N. Harmon and K. Leptokaropoulos acknowledge funding from the Natural Environment Research Council (NE/M003507/1) and the European Research Council (GA 638665). J.-M. Kendall was funded by the Natural Environment Research Council (NE/M004643/1). D. Schlaphorst was supported by the Portuguese Science and Technology Foundation (FCT/Fundação para a Ciência e Tecnologia), under project PTDC/CTA-GEF/30264/2017 and UIDB/50019/2020 – IDL. We thank the captain and crew of the R/V *Marcus G. Langseth* and the RRS *Discovery*, and also the scientific technicians. We thank William Wilcock and an anonymous reviewer, the Associate Editor and Editor, Rachel Abercrombie, for their insightful suggestions and comments.

References

Agius, M. R., Harmon, N., Rychert, C. A., Tharimena, S., & Kendall, J. M. M. (2018). Sediment characterization at the equatorial Mid-Atlantic Ridge from P-to-S teleseismic phase conversions recorded on the PI-LAB experiment. *Geophysical Research Letters*, *45*, 12244–12252. https://doi.org/10.1029/2018GL080565

Agius, M. R., Rychert, C. A., Harmon, N., Tharimena, S., & Kendall, J. M. (2021). A thin mantle transition zone beneath the equatorial Mid-Atlantic Ridge. *Nature*, *589*, 562–566. https://doi.org/10.1038/s41586-020-03139-x

Agnew, D. C. (1997). NLOADF: A program for computing ocean-tide loading. *Journal of Geophysical Research*, *102*, 5109–5110. https://doi.org/10.1029/96jb03458

Aki, K. (1965). Maximum likelihood estimate of b in the formula logN = a − bM and its confidence limits. *Bulletin of Earthquake Research Institute of the University of Tokyo*, *43*, 237–239.

Bakun, W. H., & Joyner, W. B. (1984). The ML scale in central California. *Bulletin of the Seismological Society of America*, *74*(5), 1827–1843. https://doi.org/10.1785/bssa0740051827

Barreyre, T., Escartín, J., Sohn, R. A., Cannat, M., Ballu, V., & Crawford, W. C. (2014). Temporal variability and tidal modulation of hydrothermal exit-fluid temperatures at the Lucky Strike deep sea vent field, Mid-Atlantic Ridge. *Journal of Geophysical Research: Solid Earth*, *119*, 2543–2566. https://doi.org/10.1002/2013JB010478

Behn, M. D., Boettcher, M. S., & Hirth, G. (2007). Thermal structure of oceanic transform faults. *Geology*, *35*(4), 307–310. https://doi.org/10.1130/G23112A.1

Bhatnagar, T., Tolstoy, M., & Waldhauser, F. (2015). Influence of fortnightly tides on earthquake triggering at the East Pacific Rise at 9°50′N. *Journal of Geophysical Research: Solid Earth*, *121*, 1262–1279. https://doi.org/10.1002/2015JB012388

Bogiatzis, P., Karamitrou, A., Ward Neale, J., Harmon, N., Rychert, C. A., & Srokosz, M. (2020). Source regions of infragravity waves recorded at the bottom of the equatorial Atlantic Ocean, using OBS of the PI-LAB experiment. *Journal of Geophysical Research: Oceans*, *125*, e2019JC015430. https://doi.org/10.1029/2019jc015430

Bown, J. W., & White, R. S. (1994). Variation with spreading rate of oceanic crustal thickness and geochemistry. *Earth and Planetary Science Letters*, *121*(3–4), 435–449. https://doi.org/10.1016/0012-821X(94)90082-5

Cann, J. R., Blackman, D. K., Smith, D. K., McAllister, E., Janssen, B., Mello, S., et al. (1997). Corrugated slip surfaces formed at North Atlantic ridge-transform intersections. *Nature*, *385*, 329–332. https://doi.org/10.1038/385329a0

Cannat, M. (1996). How thick is the magmatic crust at slow spreading oceanic ridges? *Journal of Geophysical Research*, *101*(B2), 2847–2857. https://doi.org/10.1029/95JB03116

Chamberlain, C. J., Hopp, C. J., Boese, C. M., Warren-Smith, E., Chambers, D., Chu, S. X., et al. (2018). EQcorrscan: Repeating and near-repeating earthquake detection and analysis in Python. *Seismological Research Letters*, *89*, 173–181. https://doi.org/10.1785/0220170151

Chatelain, J. O., Roecker, S. W., Hatzfeld, D., & Molnar, P. (1980). Microearthquake seismicity and fault plane solutions in the Hindu Kush region and their tectonic implications. *Journal of Geophysical Research*, *85*, 1365–1387. https://doi.org/10.1029/jb085ib03p01365

Christeson, G. L., Goff, J. A., & Reece, R. S. (2019). Synthesis of oceanic crustal structure from two-dimensional seismic profiles. *Reviews of Geophysics*, *57*, 504–529. https://doi.org/10.1029/2019RG000641

Cochran, E. S., Vidale, J. E., & Tanaka, S. (2004). Earth tides can trigger shallow thrust fault earthquakes. *Science*, *306*, 1164–1166. https://doi.org/10.1126/science.1103961

Dunn, R. A., Arai, R., Eason, D. E., Canales, J. P., & Sohn, R. A. (2017). Three-dimensional seismic structure of the Mid-Atlantic Ridge: An investigation of tectonic, magmatic, and hydrothermal processes in the rainbow area. *Journal of Geophysical Research: Solid Earth*, *122*, 9580–9602. https://doi.org/10.1002/2017JB015051

Egbert, G. D., & Erofeeva, S. Y. (2002). Efficient inverse modeling of barotropic ocean tides. *Journal of Atmospheric and Oceanic Technology*, *19*, 183–204. https://doi.org/10.1175/1520-0426(2002)019<0183:eimobo>2.0.co;2

Ekström, G., Nettles, M., & Dziewoński, A. M. (2012). The global CMT project 2004-2010: Centroid-moment tensors for 13,017 earthquakes. *Physics of the Earth and Planetary Interiors*, *200–201*, 1–9. https://doi.org/10.1016/j.pepi.2012.04.002

El-Isa, Z. H., & Eaton, D. W. (2014). Spatiotemporal variations in the b-value of earthquake magnitude–frequency distributions: Classification and causes. *Tectonophysics*, *615–616*, 1–11. https://doi.org/10.1016/j.tecto.2013.12.001

Escartin, J., Hirth, G., & Evans, B. (1997). Nondilatant brittle deformation of serpentinites: Implications for Mohr-Coulomb theory and the strength of faults. *Journal of Geophysical Research*, *102*, 2897–2913. https://doi.org/10.1029/96jb02792

Escartin, J., Hirth, G., & Evans, B. (2001). Strength of slightly serpentinized peridotites: Implications for the tectonics of oceanic lithosphere. *Geology*, *29*, 1023–1026. https://doi.org/10.1130/0091-7613(2001)029<1023:sosspi>2.0.co;2

Fang, W. W., Langseth, M. G., & Schultheiss, P. J. (1993). Analysis and application of in situ pore pressure measurements in marine sediments. *Journal of Geophysical Research*, *98*(B5), 7921–7938. https://doi.org/10.1029/93jb00153

Früh-Green, G. L., Plas, A., & Lécuyer, C. (1996). 14. Petrologic and stable isotope constraints on hydrothermal alteration and serpentinization of the EPR shallow mantle at Hess deep (site 895). *Proceedings of the Ocean Drilling Program, Scientific Results*, *147*, 255–291.

Gibbons, S. J., & Ringdal, F. (2006). The detection of low magnitude seismic events using array-based waveform correlation. *Geophysical Journal International*, *165*, 149–166. https://doi.org/10.1111/j.1365-246X.2006.02865.x

Grevemeyer, I., Reston, T. J., & Moeller, S. (2013). Microseismicity of the Mid-Atlantic Ridge at 7°S-8°15'S and at the Logatchev Massif oceanic core complex at 14°40'N-14°50'N. *Geochemistry, Geophysics, Geosystems*, *14*, 3532–3554. https://doi.org/10.1002/ggge.20197

Harmon, N., Rychert, C., Agius, M., Tharimena, S., Le Bas, T., Kendall, J. M., & Constable, S. (2018). Marine geophysical investigation of the Chain Fracture Zone in the equatorial Atlantic from the PI-LAB experiment. *Journal of Geophysical Research: Solid Earth*, *123*, 11016–11030. https://doi.org/10.1029/2018JB015982

Harmon, N., Rychert, C. A., Kendall, J. M., Agius, M., Bogiatzis, P., & Tharimena, S. (2020). Evolution of the oceanic lithosphere in the equatorial Atlantic from Rayleigh wave tomography, evidence for small-scale convection from the PI-LAB experiment. *Geochemistry, Geophysics, Geosystems*, *21*, e2020GC009174. https://doi.org/10.1029/2020gc009174

Harmon, N., Wang, S., Rychert, C. A., Constable, S., & Kendall, J. M. (2021). Shear velocity inversion guided by resistivity structure from the PI-LAB experiment for integrated estimates of partial melt in the mantle. *Journal of Geophysical Research: Solid Earth*, *126*, e2021JB022202. https://doi.org/10.1029/2021JB022202

Harris, R. A. (1998). Introduction to special section: Stress triggers, stress shadows and implications for seismic hazard. *Journal of Geophysical Research*, *103*, 24347–24358. https://doi.org/10.1029/98jb01576

Heaton, T. H. (1975). Tidal triggering of earthquakes. *Geophysical Journal International*, *43*, 307–326. https://doi.org/10.1111/j.1365-246x.1975.tb00637.x

Heimann, S., Isken, M., Kühn, D., Sudhaus, H., Steinberg, A., Vasyura-Bathke, H., et al. (2018). *Grond - A probabilistic earthquake source inversion framework*. V. 1.0. Potsdam: GFZ Data Services. https://doi.org/10.5880/GFZ.2.1.2018.003

Heimann, S., Kriegerowski, M., Isken, M., Cesca, S., Daout, S., Grigoli, F., et al. (2017). *Pyrocko -an open-source seismology toolbox and library*. Potsdam: GFZ Data Services. https://doi.org/10.5880/GFZ.2.1.2017.001

Herrmann, M., & Marzocchi, W. (2020). Inconsistencies and lurking pitfalls in the magnitude–frequency distribution of high-resolution earthquake catalogs. *Seismological Research Letters*, *92*, 909–922. https://doi.org/10.1785/0220200337

Hicks, S. P., Okuwaki, R., Steinberg, A., Rychert, C., Harmon, N., Abercrombie, R., et al. (2020). Back-propagating supershear rupture in the 2016 Mw 7.1 Romanche transform fault earthquake. *Nature Geoscience*, *13*, 647–653. https://doi.org/10.1038/s41561-020-0619-9

Hilmo, R., & Wilcock, W. S. D. (2020). Physical sources of high-frequency seismic noise on Cascadia Initiative ocean bottom seismometers. *Geochemistry, Geophysics, Geosystems*, *21*, e2020GC009085. https://doi.org/10.1029/2020GC009085

Hofmann, A. W. (1997). Mantle geochemistry: The message from oceanic volcanism. *Nature*, *385*, 219–229. https://doi.org/10.1038/385219a0

Horning, G., Sohn, R. A., Canales, J. P., & Dunn, R. A. (2018). Local seismicity of the Rainbow massif on the Mid-Atlantic Ridge. *Journal of Geophysical Research: Solid Earth*, *123*, 1615–1630. https://doi.org/10.1002/2017JB015288

Hough, S. E., & Kanamori, H. (2002). Source properties of earthquakes near the Salton Sea triggered by the 16 October 1999 M 7.1 Hector Mine, California, Earthquake. *Bulletin of the Seismological Society of America*, *92*(4), 1281–1289. https://doi.org/10.1785/0120000910

Ide, S., Yabe, S., & Tanaka, Y. (2016). Earthquake potential revealed by tidal influence on earthquake size–frequency statistics. *Nature*, *9*, 834–837. https://doi.org/10.1038/NGEO2796

Laske, G., Masters, G., Ma, Z., & Pasyanos, M. (2013). Update on CRUST1.0—A 1-degree global model of Earth's crust. *Geophysical Research Abstracts*, *15*, 2658.

Leptokaropoulos, K. (2020). Magnitude distribution complexity and variation at the Geysers geothermal field. *Geophysical Journal International*, *222*, 893–906. https://doi.org/10.1093/gji/ggaa208

Leptokaropoulos, K., Adamaki, A. A., Roberts, R. G., Gkarlaouni, C. G., & Paradisopoulou, P. M. (2018). Impact of magnitude uncertainties on seismic catalogue properties. *Geophysical Journal International*, *213*, 940–951. https://doi.org/10.1093/gji/ggy023

Leptokaropoulos, K., & Lasocki, S. (2020). SHAPE: A Matlab software package for time-dependent seismic hazard analysis. *Seismological Research Letters*, *91*, 1867–1877. https://doi.org/10.1785/0220190319

Linker, J., & Dieterich, J. (1992). Effects of variable normal stress on rock friction: Observations and constitutive equations. *Journal of Geophysical Research*, *97*, 4923–4940. https://doi.org/10.1029/92JB00017

Lomax, A., Virieux, J., Volant, P., & Berge-Thierry, C. (2000). Probabilistic earthquake location in 3D and layered models. *Advances in Seismic Event Location*, *18*, 101–134. https://doi.org/10.1007/978-94-015-9536-0_5

Macdonald, K. C. (2001). Mid-ocean ridge tectonics, volcanism and geomorphology. In J. Steele, S. Thorpe, & K. Turekian (Eds.), *Encyclopedia of ocean sciences* (pp. 1798–1813). Academic Press. https://doi.org/10.1006/rwos.2001.0094

Marjanović, M., Singh, S. C., Gregory, E. P. M., Grevemeyer, I., Growe, K., Wang, Z., et al. (2020). Seismic crustal structure and morphotectonic features associated with the Chain Fracture Zone and their role in the evolution of the equatorial Atlantic region. *Journal of Geophysical Research: Solid Earth*, *125*, e2020JB020275. https://doi.org/10.1029/2020JB020275

Marsaglia, G., & Marsaglia, J. (2004). Evaluating the Anderson-Darling distribution. *Journal of Statistical Software*, *9*, 1–5. https://doi.org/10.18637/jss.v009.i02

Mercier, H., & Morin, P. (1997). Hydrography of the Romanche and Chain Fracture Zones. *Journal of Geophysical Research*, *102*(C5), 10373–10389. https://doi.org/10.1029/97JC00229

Mercier, H., & Speer, K. G. (1998). Transport of bottom water in the Romanche Fracture Zone and the Chain Fracture Zone. *Journal of Physical Oceanography*, *28*(5), 779–790. https://doi.org/10.1175/1520-0485(1998)028<0779:Tobwit>2.0.Co;2

Minson, S. E., Dreger, D. S., Bürgmann, R., Kanamori, H., & Larson, K. M. (2007). Seismically and geodetically determined nondouble-couple source mechanisms from the 2000 Miyakejima volcanic earthquake swarm. *Journal of Geophysical Research*, *112*, B10308. https://doi.org/10.1029/2006JB004847

Parnell-Turner, R., Sohn, R. A., Peirce, C., Reston, T. J., Macleod, C. J., Searle, R. C., & Simão, N. M. (2017). Oceanic detachment faults generate compression in extension. *Geology*, *45*, 923–926. https://doi.org/10.1130/g39232.1

Parnell-Turner, R., Sohn, R. A., Peirce, C., Reston, T. J., Macleod, C. J., Searle, R. C., & Simão, N. M. (2020). Seismicity trends and detachment fault structure at 13°N, Mid-Atlantic Ridge. *Geology*, *49*, 320–324. https://doi.org/10.1130/G48420.1

Rice, J. R., & Cleary, M. P. (1976). Some basic stress diffusion solutions for fluid-saturated elastic porous media with compressible constituents. *Reviews of Geophysics*, *14*, 227–241. https://doi.org/10.1029/rg014i002p00227

Rychert, C., Kendall, J. M., & Harmon, N. (2016). *Passive imaging of the lithosphere-asthenosphere boundary [data set]*. International Federation of Digital Seismograph Networks. https://doi.org/10.7914/SN/XS_2016

Rychert, C. A., Harmon, N., Constable, S., & Wang, S. (2020). The nature of the lithosphere-asthenosphere boundary. *Journal of Geophysical Research: Solid Earth*, *125*, e2018JB016463. https://doi.org/10.1029/2018JB016463

Rychert, C. A., Tharimena, S., Harmon, N., Wang, S., Constable, S., Kendall, J. M., et al. (2021). A dynamic lithosphere–asthenosphere boundary near the equatorial Mid-Atlantic Ridge. *Earth and Planetary Science Letters*, *566*, 116949. https://doi.org/10.1016/j.epsl.2021.116949

Saikia, U., Rychert, C., Harmon, N., & Kendall, J. M. (2020). Sediment structure at the equatorial Mid-Atlantic ridge constrained by seafloor admittance using data from the PI-LAB experiment. *Marine Geophysical Research*, *41*, 3. https://doi.org/10.1007/s11001-020-09402-0

Saikia, U., Rychert, C., Harmon, N., & Kendall, J. M. (2021). Upper mantle anisotropic shear velocity structure at the equatorial Mid-Atlantic Ridge constrained by Rayleigh wave group velocity analysis from the PI-LAB experiment. *Geochemistry, Geophysics, Geosystems*, *22*, e2020GC009495. https://doi.org/10.1029/2020GC009495

Scholz, C. H., Tan, Y. J., & Albino, F. (2019). The mechanism of tidal triggering of earthquakes at mid-ocean ridges. *Nature*, *10*, 2526. https://doi.org/10.1038/s41467-019-10605-2

Schuster, A. (1897). On lunar and solar periodicities of earthquakes. *Proceedings of the Royal Society of London*, *61*, 455–465. https://doi.org/10.1098/rspl.1897.0060

Simpson, R. W., & Reasenberg, P. A. (1994). Earthquake-induced static stress changes on central California faults. In R. W. Simpson (Ed.), *The loma prieta, California earthquake of October 17, 1989-tectonic processes and models* (Vol. 1550-F, pp. F55–F89). U.S. Geol. Surv. Prof. Pap.

Singh, S., Crawford, W., Carton, H., Seher, T., Combier, V., Cannat, M., et al. (2006). Discovery of a magma chamber and faults beneath a Mid-Atlantic Ridge hydrothermal field. *Nature*, *442*, 1029–1032, https://doi.org/10.1038/nature05105

Skempton, A. W. (1954). The pore-pressure coefficients A and B. *Géotechnique*, *4*, 143–147. https://doi.org/10.1680/geot.1954.4.4.143

Stroup, D. F., Bohnenstiehl, D. R., Tolstoy, M., Waldhauser, F., & Weekly, R. T. (2007). Pulse of the seafloor: Tidal triggering of microearthquakes at 9 degrees 50'N East Pacific Rise. *Geophyical Research Letters*, *34*, L15301. https://doi.org/10.1029/2007gl030088

Stroup, D. F., Tolstoy, M., Crone, T. J., Malinverno, A., Bohnenstiehl, D. R., & Waldhauser, F. (2009). Systematic along-axis tidal triggering of microearthquakes observed at 9°50'N East Pacific Rise. *Geophysical Research Letters*, *36*, L18302. https://doi.org/10.1029/2009GL039493

Sykes, L. R. (1970). Earthquake swarms and sea-floor spreading. *Journal of Geophysical Research*, *75*, 6598–6611. https://doi.org/10.1029/jb075i032p06598

Tan, Y. J., Tolstoy, M., Waldhauser, F., & Bohnenstiehl, D. R. (2018). Tidal triggering of microearthquakes over an eruption cycle at 9°50'N East Pacific Rise. *Geophysical Research Letters*, *45*, 1825–1831. https://doi.org/10.1002/2017GL076497

Tan, Y. J., Waldhauser, F., Tolstoy, M., & Wilcock, W. S. D. (2019). Axial Seamount: Periodic tidal loading reveals stress dependence of the earthquake size distribution (bvalue). *Earth and Planetary Science Letters*, *512*, 39–45. https://doi.org/10.1016/j.epsl.2019.01.047

Tanaka, S., Ohtake, M., & Sato, H. (2002). Evidence for tidal triggering of earthquakes as revealed from statistical analysis of global data. *Journal of Geophysical Research*, *107*(B10), 2211. https://doi.org/10.1029/2001JB001577

Tesei, T., Harbord, C. W. A., De Paola, N., Collettini, C., & Viti, C. (2018). Friction of mineralogically controlled serpentinites and implications for fault weakness. *Journal of Geophysical Research: Solid Earth*, *123*, 6976–6991. https://doi.org/10.1029/2018JB016058

Teza, E., Scordilis, E. M., Papazachos, C. B., & Karakaisis, G. F. (2016). An earthquake catalog of Mid-Atlantic Ridge. *Bulletin of the Geological Society of Greece*, *50*, 1258–1269. https://doi.org/10.12681/bgsg.11832

Tolstoy, M., Vernon, F. L., Orcutt, J. A., & Wyatt, F. K. (2002). Breathing of the seafloor: Tidal correlations of seismicity at Axial volcano. *Geology*, *30*(6), 503–506. https://doi.org/10.1130/0091-7613(2002)030<0503:botstc>2.0.co;2

Tsuruoka, H., Ohtake, M., & Sato, H. (1995). Statistical test of the tidal triggering of earthquakes: Contribution of the ocean tide loading effect. *Geophysical Journal International*, *122*(1), 183–194. https://doi.org/10.1111/j.1365-246x.1995.tb03546.x

Utsu, T. (1999). Representation and analysis of the earthquake size distribution: A historical review and some new approaches. *Pure and Applied Geophysics*, *155*, 509–535. https://doi.org/10.1007/s000240050276

van der Elst, N. J. (2021). B-positive: A robust estimator of aftershock magnitude distribution in transiently incomplete catalogs. *Journal of Geophysical Research: Solid Earth*, *126*, e2020JB021027. https://doi.org/10.1029/2020JB021027

Vidale, J. E., Agnew, D. C., Johnston, M. J. S., & Oppenheimer, D. H. (1998). Absence of earthquake correlation with Earth tides: An indication of high preseismic fault stress rate. *Journal of Geophysical Research*, *103*(B10), 24567–24572. https://doi.org/10.1029/98jb00594

Vuan, A., Sugan, M., Amati, G., & Kato, A. (2018). Improving the detection of low-magnitude seismicity preceding the Mw 6.3 L'Aquila Earthquake: Development of a scalable code based on the cross correlation of template earthquakes. *Bulletin of the Seismological Society of America*, *108*, 471–480. https://doi.org/10.1785/0120170106

Waldhauser, F., & Ellsworth, W. L. (2000). A double-difference earthquake location algorithm; method and application to the northern Hayward Fault, California. *Bulletin of the Seismological Society of America*, *90*, 1353–1368. https://doi.org/10.1785/0120000006

Wang, S., Constable, S., Rychert, C. A., & Harmon, N. (2020). A lithosphere-asthenosphere boundary and partial melt estimated using marine magnetotelluric data at the central Middle Atlantic Ridge. *Geochemistry, Geophysics, Geosystems*, *21*, e2020GC009177. https://doi.org/10.1029/2020GC009177

Wilcock, W. S. D. (2001). Tidal triggering of micro earthquakes on the Juan de Fuca Ridge. *Geophysical Research Letters*, *28*, 3999–4002. https://doi.org/10.1029/2001gl013370

Wilcock, W. S. D. (2009). Tidal triggering of earthquakes in the Northeast Pacific Ocean. *Geophysical Journal International*, *179*, 1055–1070. https://doi.org/10.1111/j.1365-246X.2009.04319.x

Wilcock, W. S. D., Tolstoy, M., Waldhauser, F., Garcia, C., Tan, Y. J., Bohnenstiehl, D. R., et al. (2016). Seismic constraints on caldera dynamics from the 2015 Axial Seamount eruption. *Science*, *354*, 1395–1399. https://doi.org/10.1126/science.aah5563

Reference From the Supporting Information

Richter, C. F. (1958). *Elementary seismology* (p. 578). San Francisco, California: W. H. Freeman and Co.